



**QUEEN'S
UNIVERSITY
BELFAST**

Direct and indirect band gaps in Ge under biaxial tensile strain investigated by photoluminescence and photoreflectance studies

Saladukha, D., Clavel, M. B., Murphy-Armando, P., Greene-Diniz, G., Gruening, M., Hudait, M. K., & Ochalski, T. J. (2018). Direct and indirect band gaps in Ge under biaxial tensile strain investigated by photoluminescence and photoreflectance studies. *Physical Review B*, 97(19), [195304]. <https://doi.org/10.1103/PhysRevB.97.195304>

Published in:
Physical Review B

Document Version:
Peer reviewed version

Queen's University Belfast - Research Portal:
[Link to publication record in Queen's University Belfast Research Portal](#)

Publisher rights

© 2018 American Physical Society. This work is made available online in accordance with the publisher's policies. Please refer to any applicable terms of use of the publisher.

General rights

Copyright for the publications made accessible via the Queen's University Belfast Research Portal is retained by the author(s) and / or other copyright owners and it is a condition of accessing these publications that users recognise and abide by the legal requirements associated with these rights.

Take down policy

The Research Portal is Queen's institutional repository that provides access to Queen's research output. Every effort has been made to ensure that content in the Research Portal does not infringe any person's rights, or applicable UK laws. If you discover content in the Research Portal that you believe breaches copyright or violates any law, please contact openaccess@qub.ac.uk.

Direct and Indirect Ge energy bands under biaxial tensile strain investigated by photoluminescence and photoreflectance studies.

D. Saladukha^{1,2}, M. B. Clavel³, F. Murphy-Armando², G. Greene-Diniz⁴, M. Gruening⁴, M. K. Hudait³, T. J. Ochalski^{1,2}.

¹Centre for Advanced Photonics and Process Analysis, Cork Institute of Technology, Cork, Ireland

²Tyndall National Institute, Lee Maltings, Dyke Parade, Cork, Ireland

³Advanced Devices & Sustainable Energy Laboratory (ADSEL), Bradley Department of Electrical and Computer Engineering, Virginia Tech, Blacksburg, Virginia 24061, USA

⁴Atomistic Simulation Centre, School of Mathematics and Physics, Queen's University Belfast, University Road, Belfast BT7 1NN, Northern Ireland, United Kingdom

Abstract

Germanium is an indirect semiconductor which attracts a particular interest as an electronics and photonics material due to low indirect to direct band separation. In this work we bend the bands of Ge by means of biaxial tensile strain in order to achieve a direct bandgap. Strain is applied by growth of Ge on a lattice mismatched InGaAs buffer layer with variable In content. Band structure is studied by photoluminescence and photoreflectance, giving the indirect and direct bands of the material. Obtained experimental energy band values are compared with a k·p simulation. Photoreflectance spectra are also simulated and compared with the experiment. The obtained results indicate direct band structure obtained for a Ge sample with 1.94 % strain applied, with preferable Γ -valley to heavy hole transition.

Introduction

In recent years there has been extensive on-going research in the field of optical interconnects¹⁻³. However an integrated laser-on-a-chip still faces the bottleneck of different substrate materials typically used in current industrial processes for lasers and transistor structures. There are different approaches proposed to combine these substrates such as flip-chip^{2,4} or wafer bonding⁵⁻⁷. Other approaches propose growth of both the laser and transistor structures on a single chip. Some success was reported on InP substrates,^{8,9} but the high cost of InP wafers is discouraging for broader applications. Growth of a laser directly on a Si substrate encounters challenges given by the lattice mismatch between common laser materials and Si. However there are a number of interesting results in this field obtained by growth of a buffer GaAs layer on a Si substrate¹⁰ and by growth of materials with similar lattice parameters, such as GeSn¹¹⁻¹³.

Germanium is a promising material for both photonic and electronic applications. It is an indirect gap semiconductor, but has a direct band valley merely 0.14 eV above the conduction band. This band can be lowered in energy by applying tensile strain to Ge^{14,15}, turning it into a direct gap semiconductor. This method can also be applied to boost charge carrier mobility^{16–18}, which has a profound effect on transistor switch rate and is critical for electronic applications. When attempting to increase power density on a chip through miniaturization of the next generation of transistors, heat dissipation becomes challenging in standard MOSFETs. Heat is generated not only by transistors, but also by the connection wires. Instead, increasing the transistor switch rate allows keeping the same wiring with an increase of overall processor clock rate. Also Ge FETs are candidates for low voltage stage gap transistors¹⁹. These properties of Ge will provide low energy consumption with easier heat dissipation than existing Si technology. In this paper, we study the band of Ge under biaxial tensile strain, applied by growth of Ge on a lattice mismatched In_xGa_{1-x}As layer, by means of photoluminescence (PL) and photorefectance (PR) studies. In the beginning we describe the theoretical model of Ge crystal used to calculate energy levels and electron-hole wavefunctions coupling in the crystal under various strain and temperatures. In the next section we describe growth conditions of the studied samples. This is followed by the experimental methods, PL and PR in particular, including the theory used for spectra interpretation. The main section presents and discusses the results obtained from the experiment and the theoretical modelling, with a short summary in the conclusion section.

Theoretical model of strained Ge

The quantum well energy levels and optical coupling between conduction and valence bands were calculated as follows:

We used the 30 band k·p approach that includes the effects of strain from D. Rideau *et al*²⁰, which is based on experiment and GW²¹ calculations. We added the temperature dependence of the *L* and *Γ* bands to this model from experiments²².

The quantum confinement was solved using the envelope approximation numerically, using the k·p Hamiltonian mentioned above. The boundary conditions were given by the experimental values of the band gap and effective masses of InGaAs and the calculated band-offsets from Ref²³.

We used the boundary matching conditions from W.A. Harrison²⁴. The temperature dependence of the energy gaps in InGaAs is taken from Ref²⁵.

The latter approach gives permitted crystal momentum k values for the $k \cdot p$ model. The optical coupling constants are extracted from the momentum operator between the wave-function of the permitted states in the $k \cdot p$ model:

$$\langle \psi_{k_i} | \hat{\mathbf{p}} | \psi_{k_f} \rangle = \frac{m_0}{\hbar} \langle u_{k_i} | \hat{\mathbf{p}} \cdot \nabla_k H | u_{k_f} \rangle \int dz \phi_{k_i}^*(z) \phi_{k_f}(z) \quad (1.1)$$

Where ϕ and u are the envelope and Bloch functions, respectively.

The generation rate of direct band gap photons goes as:

$$R_{dir} = \frac{2\pi}{\hbar} \left| \langle \psi_{k_i} | \hat{\mathbf{p}} | \psi_{k_f} \rangle \right|^2 \delta(E_f - E_i) \quad (1.2)$$

The generation rate of indirect phonons is given by:

$$R_{ind} = \frac{2\pi}{\hbar} \sum_{k_i, k_f} \left| \sum_j \frac{\langle \psi_f | H_{el-ph} | \psi_j \rangle \langle \psi_j | \hat{\mathbf{p}} | \psi_i \rangle}{E_j - E_i - \hbar\nu} \right|^2 \delta(E_f - E_i - \hbar\nu - \hbar\omega) \quad (1.3)$$

The electron phonon coupling H_{el-ph} between the L and Γ bands has been calculated in Ref¹⁸.

The Seraphin-Bottka coefficients used to fit the photoreflectance spectra are extracted from first principles simulations of the real and imaginary parts of the macroscopic dielectric function ϵ_m . The latter is calculated within a linear response independent particle framework. The local density approximation (LDA) to Kohn-Sham Density Functional Theory (DFT) is used along with plane wave basis sets and pseudopotentials. A self-consistent ground state²⁶⁻²⁸ for the minimum energy geometry is calculated at a plane wave kinetic energy cutoff of 50 Rydbergs, and a grid of $12 \times 12 \times 12$ k -points used to sample the Brillouin Zone. The energy gap at the Γ point is subsequently corrected with the GW approximation^{21,29} (where G is the independent particle Green's function and W is the dynamically screened Coulomb interaction) using numerically converged numbers of unoccupied states and off-diagonal elements in the dielectric response function. The GW correction yields realistic optical transition energies which are used to calculate ϵ_m from the expression²⁹:

$$\varepsilon_m^{-1}(\omega) = 1 + \lim_{q \rightarrow 0} \frac{4\pi}{|q^2|} \chi_{G=0, G'=0}(\mathbf{q}, \omega), \quad (1.4)$$

where \mathbf{q} is an arbitrary wave vector, \mathbf{G} is a reciprocal lattice vector. The $\mathbf{q} \rightarrow \mathbf{0}$ limit is taken due to the extremely small momentum, relative to the crystal momentum, carried by a photon. The response function χ is calculated using the Kohn-Sham wavefunctions (these are obtained from a finer grid of $24 \times 24 \times 24$ k-points when calculating ε_m) and the independent particle Green's function G^{29} . Local-field effects ($\chi_{(G \neq 0, G' \neq 0)}$) have a negligible effect on ε_m up to ~ 1.5 eV above the valence band edge, and given the energy range used for the Seraphin-Bottka coefficients (see Figure A3 in the Appendix), the extra computational load of including local field effects in the response function is avoided and only diagonal elements of χ are obtained for the optical spectra. In addition, $\chi(\omega)$ is corrected by a material dependent factor (a) which partially accounts for the variations in the response function (relative to an independent particle framework) due to the static long range contribution to the exchange correlation kernel, yielding improved lineshapes for optical spectra in better agreement with experiment^{30,31}. The corrected response function χ_a is obtained from

$$\chi_a^{-1} = \chi^{-1} - a \quad (1.5)$$

and a is related to the static dielectric constant as

$$a = \frac{1}{\chi(\omega=0)\varepsilon_m(\omega=0)}. \quad (1.6)$$

Once the real ($n = \frac{1}{\sqrt{2}} \left[\varepsilon_1 + \sqrt{(\varepsilon_1^2 + \varepsilon_2^2)} \right]^{1/2}$) and imaginary parts ($k = \frac{1}{\sqrt{2}} \left[\sqrt{(\varepsilon_1^2 + \varepsilon_2^2)} - \varepsilon_1 \right]^{1/2}$) of the refractive index are calculated from the real (ε_1) and imaginary (ε_2) parts of ε_m ,³² the Seraphin-Bottka coefficients α and β can be obtained from the relations^{33,34}:

$$\alpha = \frac{2A}{A^2 + B^2}, \quad (1.7)$$

and

$$\beta = \frac{2B}{A^2 + B^2}. \quad (1.8)$$

Where the quantities A and B are related to n and k as

$$A = n(n^2 - 3k^2 - 1), \quad (1.9)$$

and

$$B = k(3n^2 - k^2 - 1). \quad (1.10)$$

In previous works, these relations between the Seraphin-Bottka coefficients and ϵ_m have been used by Sundari and Raghavan³⁴ to evaluate the degree of disorder present in experimental samples of tetrahedrally bonded semiconductors, and by Bondi et al³³ to assess the contribution to optical spectra of suboxide composition and bonding disorder in oxide terminated Si nanowires. In this work, they provide a convenient way to extract parameters for experimental photoreflectance spectra, starting only from plane wave pseudopotential DFT calculations.

Material Synthesis

The unintentionally doped epitaxial Ge thin films investigated in this work were grown using a dual-chamber, solid-source molecular beam epitaxy (MBE) growth process. To this end, separate group IV and III-V reactors, connected *via* an ultra-high vacuum transfer chamber, were utilized in order to minimize interatomic diffusion and cross-species contamination during growth³⁵. Starting substrates of either (001)GaAs or (001)Si, offcut 2° to 6° towards the [110] direction in order to minimize the formation of anti-phase domain boundaries,^{36,37} were first desorbed of native oxide at 750 °C and 940 °C, respectively, noting that GaAs native oxide desorption was performed under an $\sim 1 \times 10^{-5}$ Torr As₂ overpressure. For samples utilizing GaAs substrates, a 0.25 μm homoepitaxial GaAs buffer was grown at 650°C (0.5 $\mu\text{m}/\text{hour}$ growth rate) following native oxide desorption, thereby creating an atomically-flat growth surface for subsequent epitaxy. For samples utilizing Si substrates, a multi-step, cyclically-annealed 2.0 μm GaAs metamorphic buffer was grown so as to bridge the lattice constants between GaAs and Si and mitigate the propagation of defects and dislocations within subsequent epitaxial III-V and Ge layers. Following GaAs buffer growth, an up to 1.9 μm linearly graded In_xGa_{1-x}As metamorphic buffer was grown at 550°C, wherein the thickness and strain grading rate were selected based on the desired strain-state of the overlying Ge epilayer, and thus Indium (In) composition of the subsequent constant-composition In_xGa_{1-x}As stressor. Specifically, In stressor compositions of 11 %, 15 %, 17 %, 24 %, and 29 % were selected (samples B, C, D, E, and F, respectively), corresponding to empirical strain states of 0.82 %, 0.95 %, 1.11 %, 1.6 %, and 1.94 %, respectively, as determined *via* x-ray diffraction analysis and independently confirmed using Raman spectroscopy³⁸⁻⁴⁰. Upon completion of the In_xGa_{1-x}As stressor, the samples were gradually cooled to 100°C and immediately transferred *in vacuo* to the group IV growth chamber. Thin 15 nm to 240 nm Ge epilayers were then grown at

400°C utilizing a low Ge growth rate of ~ 0.025 $\mu\text{m}/\text{hour}$ and finally cooled to room temperature following growth at a rate of 5 $^{\circ}\text{C}$ per minute, thereby minimizing relaxation and unintentional thermal stress accumulation due to the mismatch in thermal expansion coefficients between materials. Unstrained epitaxial Ge controls (sample A) were also grown on (001)GaAs and (001)Si utilizing the aforementioned procedures with the substitution of a 170 nm AlAs isolation layer grown at 600 $^{\circ}\text{C}$ (0.17 $\mu\text{m}/\text{hour}$ growth rate) preceding the GaAs metamorphic buffer growth. Complete growth and materials characterization details, including sample-specific capping layer growth (samples C, D, and F) and Ge critical thickness considerations, are reported elsewhere.^{35,38–}

40

Experimental Methods

Low temperature photoluminescence (PL) was utilized to obtain band gap information of the designed materials. For sample excitation, a Ti:Sa pulsed laser was used with a power of 0.4 W, focused on a 6 μm spot at the sample surface, giving 1.4 MW/cm^2 . Samples were held inside a liquid nitrogen cryostat with temperature range from 80 K to 300 K. Emission of the sample was focused through a longpass filter to a monochromator equipped with a liquid nitrogen chilled InAs detector. For sample surface monitoring and precise focusing, a CCD camera with an external LED source was used during alignment, similar to a confocal microscope setup. This arm was inserted in the setup with the help of a removable 50/50 beamsplitter placed prior to the focusing objective and the sample holder. This beamsplitter was removed after alignment, providing full PL focused on the monochromator slit.

The photoreflectance⁴¹ technique was used to study transition energies above the band edge. A 405 nm, 40 mW laser diode was used to perturb an electric field at the surface of the material. This results in perturbation of the complex dielectric function of the semiconductor, which in turn defines the reflectance of the semiconductor.

Broadband tungsten light source is placed in one entrance of the monochromator slit to provide a wavelength range for a reflection spectrum of the sample. Liquid nitrogen chilled detector with a longpass filter was used to measure the reflection response.

A longpass filter was used to cut any emission at wavelength shorter than 1 μm and avoid second order diffraction peaks in the spectra. A combination of longpass filters was also used to study

spectra in the 0.7-1.4 μm range and the 1.3-2.6 μm range. All samples were placed in a liquid nitrogen cryostat and chilled to 80 K.

The standard chopper modulation technique allowed tracking of the changes in reflectance with and without perturbation. This setup configuration provided detection of the photorefectance signal with no influence of the PL on the spectral shape. Photorefectance spectra were fitted using Franz-Keldysh (FKO) oscillation⁴² and third order derivative lineshape (TDLS).

The (FKO) model is based on the complex Airy functions and was explained in detail by Estrera⁴³, Seraphin and Bottka⁴⁴, Aspnes⁴⁵ and Batchelor⁴⁶. Based on their research we used the following set of equations:

$$\frac{\Delta R}{R} = \text{Re} \left(C e^{i\varphi} \frac{H(z)}{(E - i\Gamma)^2} \right), \quad (2.1)$$

$$\tan \varphi = -\frac{\beta}{\alpha}, \quad (2.2)$$

$$H(z) = F(z) + iG(z), \quad (2.3)$$

$$z = \frac{1}{\hbar\theta} (E - E_c) + i\Gamma, \quad (2.4)$$

$$\Gamma = \Gamma_0 \exp((E_c - E)\delta) \quad (2.5)$$

Parameter C is a combination of amplitude parameters; $\tan \varphi$ represents ratio of Seraphin- Bottka coefficients α and β ; Γ is a broadening parameter in energy units, related to the lifetime of charge carriers, and amplitude Γ_0 - a modified nominal broadening at transition energy; δ is the Batchelor's fitting parameter, related to defects in the structure; E_c is the critical energy of the transition; $\hbar\theta$ is related to the lattice perturbation strength in the lattice:

$$\hat{U}_{\text{eff}} = \frac{2\mu_{\parallel}}{e\hbar} (\hbar\theta)^{3/2}, \quad (2.6)$$

where e is an electron charge; μ_{\parallel} is a joint interband effective mass of the solid and \mathcal{E}_{eff} is an effective built-in electric field in the lattice.

The functions F and G are electro-optics functions of the first and second kind⁴⁵ :

$$F(x) = \pi \left(Ai'(x) Ai'(x) - x Ai(x) Ai(x) \right) - u(-x) \sqrt{-x}, \quad (2.7)$$

$$G(x) = \pi \left(Ai'(x) Bi'(x) - x Ai(x) Bi(x) \right) - u(x) \sqrt{x}, \quad (2.8)$$

where $Ai(x)$ is the Airy function and $Ai'(x)$ is its derivative and $u(x)$ represents the unit step function, taking a value of 1 for positive x and 0 elsewhere. It should be noted that the critical point $E=E_c$ is omitted from the fit due to resultant infinities in F and G .

The TDLS approximation was first used for PR approximation by Aspnes⁴⁷. He stated that in the case of low perturbation field, the relative change in reflection can be defined by:

$$\frac{\Delta R}{R} = Re \left(\frac{C}{E^2} e^{i\varphi} (E - E_c + i\Gamma)^{-n} \right), \quad (2.9)$$

where C , Γ and φ have similar meaning to the definitions above; $n=3$ for two-dimensional parabolic model densities of states. In his work Aspnes omits the terms corresponding to $1/E^2$, however in the case of large broadening it can play a significant role and hence we included it in the model.

A simplified TDLS model is often used,⁴⁸⁻⁵⁰ but it is valid only in the case of low and uniform electrical perturbation of the crystal material^{51,52}. Low perturbation can be estimated from the experiment as the case of $\Delta R/R \leq 10^{-4}$.⁴⁷

Any source of background noise, such as PL, can generate an offset on the PR spectra $dR+R_0$. This offset is normally compensated by the lock-in, but can have some effect on the graph. For this purpose, an offset parameter R_0 was added to the fitting.

Results and Discussions

In this work, Ge samples with applied biaxial tensile strain from 0 % to 1.94 % are studied. Ge strain, structure and thickness parameters are summarised in Table 1. Some samples (C, F) have a GaAs or InGaAs capping layer grown over the strained Ge and are used only in the PL analysis.

Table 1. Description of Ge sample structures

Sample	Strain (%)	Cap	Structure	Ge thickness (nm)
A	0	No	Ge	bulk
B	0.82	No	Ge/In _{0.11} Ga _{0.89} As/GaAs/Si	40
C	0.95	Yes	GaAs/Ge/In _{0.16} Ga _{0.84} As/GaAs	15
D	1.11	No	Ge/In _{0.17} Ga _{0.83} As/GaAs/Si	30
E	1.6	No	Ge/In _{0.24} Ga _{0.76} As/GaAs	28
F	1.94	Yes	InGaAs/Ge/In _{0.29} Ga _{0.71} As/GaAs	15

A) Photoluminescence

Figure 1(a) depicts PL of sample A (Table 1), which is a Ge/AlAs/GaAs/Si layer structure. Ge has a 0.05 % smaller lattice parameter than AlAs, so in this sample a thick 240 nm Ge layer on a 170 nm layer of AlAs which is well above critical thickness and results in no strain ($\epsilon=0$ %).

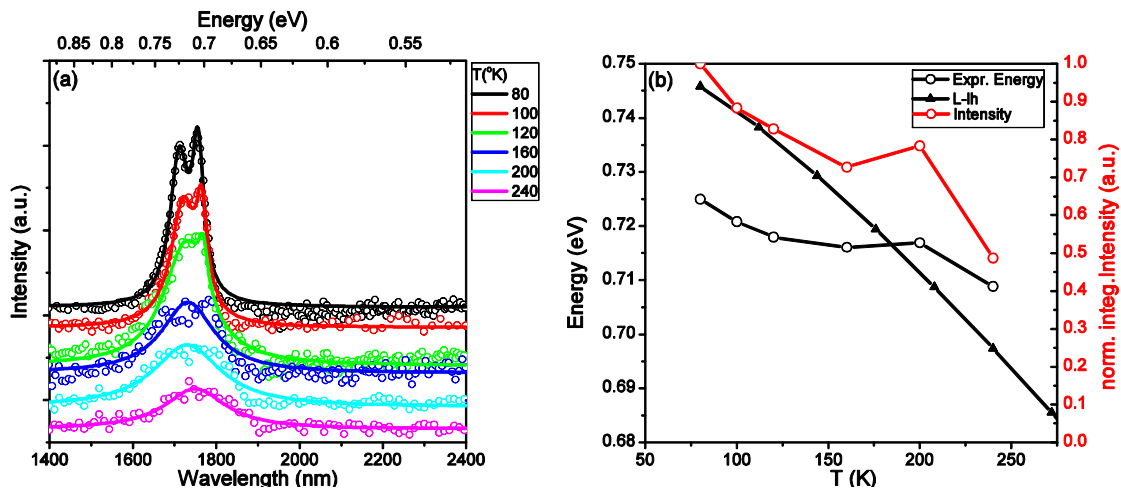


Figure 1. (a) Photoluminescence spectra of Ge/AlAs (Sample A) under $\epsilon=0$ % biaxial tensile strain depending on temperature, (b) experimental (circles) and calculated (triangles) peak energy (black line) and normalised integrated intensity (red line) versus temperature.

The peaks of the emission for this and the following PL spectra are fitted using a Lorentzian function. The sample A peaks are centered at 0.725 eV (1710 nm) and 0.706 eV (1756 nm) at 80 K. $k \cdot p$ modelling of energy bands showed the the L-valley to light holes (L-lh) transition with energy 0.746 eV. Measured peaks corresponds to longitudinal acoustic (LA) and transverse optical (TO) phonon assisted recombination, similar to reported⁵³. At low temperature there are less free phonons in the crystal, phonon-assisted recombination from the L-band generates a phonon. For this reason at low temperature emission energy is lower than energy gap with rest of recombination energy transferred into a phonon. At high temperature there are more phonons in the crystal and recombination happens after absorption of a free phonon. This results in increase of emission energy as well phonon is not generated, but absorbed. Red shift of the PL emission, as the temperature changes from 80 K to 240 K, can be seen in Fig. 1(b), corresponding to temperature dependence of the L-valley. Temperature dependence of L band is also compared with absorption experiments²².

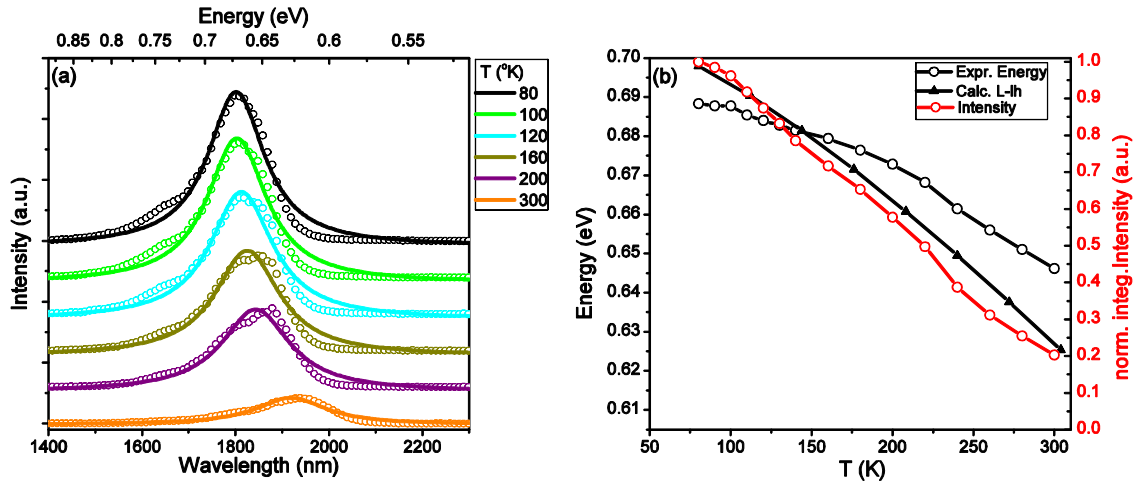


Figure 2. (a) Photoluminescence spectra of GaAs/Ge/In_{0.16}Ga_{0.84}As/GaAs (Sample C) under $\epsilon=0.95$ % biaxial tensile strain depending on temperature, (b) experimental (circles) and calculated (triangles) peak energy (black line) and normalised integrated intensity (red line) versus temperature.

Sample C (Table 1) is a structure of layers GaAs/Ge/In_{0.16}Ga_{0.84}As/GaAs with GaAs and Ge layer thickness of 15 nm each. It has an $\epsilon=0.95$ % biaxial tensile strain in the Ge layer. This sample provided bright PL, shown in Fig. 2(a). Peak emission at 80 K corresponds to 0.687 eV (1805nm) band gap energy. As can be seen there is a 40 meV (98 nm) red shift in comparison to the sample with no strain, which is expected due to the shrinking of the energy gap under tensile strain for such a thin sample. Bright emission can be explained via the compounding effects of strain-dependent gain enhancement, prohibitively large energy separations between the L and Γ

conduction band minima, and momentum contribution to the indirect L-valley light holes (lh) recombination path from exciton-generated longitudinal acoustic (LA) phonons³⁹. In the former case, several theoretical⁵⁴⁻⁵⁶ and experimental^{57,58} studies have demonstrated the effects of increasing tensile strain and doping concentrations on optical gain (or absorption) in Ge films. From these previous results, one would expect that the lower energy spectral features would exhibit higher relative PL intensities when compared with the higher energy features, as will be seen later in Fig. 5 comparing samples with 0 % and 0.95 % of strain.

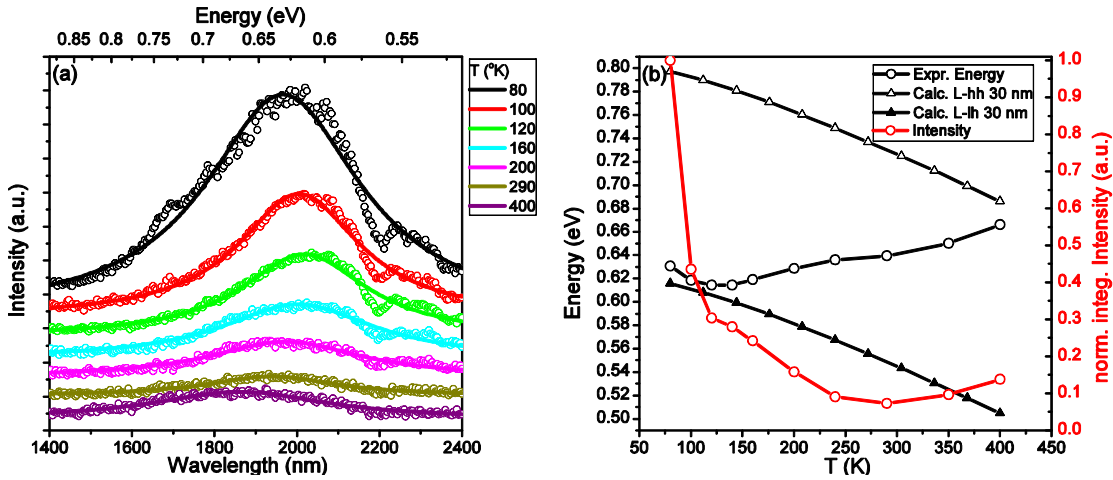


Figure 3. (a) Photoluminescence spectra of Ge/In_{0.24}Ga_{0.76}As (Sample E) under $\epsilon=1.6$ % biaxial tensile strain depending on temperature, (b) experimental (circles) and calculated (triangles) peak energy (black line) and normalised integrated intensity (red line) versus temperature.

Next, sample E (Table 1) has a similar composition with some increase in strain. This is a Ge/In_{0.24}Ga_{0.76}As/GaAs structure with Ge layer thickness of 28 nm. Biaxial tensile strain applied to Ge in this case is equal to $\epsilon=1.6$ %. The center of emission at 80 K corresponds to 0.631 eV (1944 nm). An interesting behaviour in the PL spectra is observed with increasing temperature as seen in Fig. 3(b). The PL spectra red shifts to 0.614 eV (2020 nm) at 160 K before blue shifting to 0.640 eV (1938 nm) as the temperature further increases to 290 K. Also, the broad nature of the PL emission for this sample is noticeable in Fig. 3(a). This sample corresponds to the indirect-to-direct bandgap transition point for the Ge according to 30 band $k \cdot p$ simulation shown in Fig. 8(b). Reasons for this blue shift include different charge carrier lifetimes inside the indirect L-valley and direct Γ -valley as well as the presence of nonradiative recombination inside the structure. Defects within the structure strongly suppress emission from the indirect L-valley transition, due to the slow recombination rate in the indirect channel. Indirect transitions require a phonon for

motion in k-space. For this reason, the probability of two carriers (an electron and a hole) coinciding is higher than that for 3 entities (an electron, a hole and a phonon), so transitions from the direct Γ -valley have a faster recombination rate. This also means that leakage of charge carriers through non-radiative recombination channels has less effect on direct bandgap emission compared to indirect bandgap emission. This results in domination of the direct bandgap emission at higher temperatures over the indirect and emission switch, which gives a blue shift with increase of temperature.

Another point is that according to Fermi-Dirac distribution, at higher temperatures there is a broad distribution of energies of the charge carriers and thus a higher possibility of recombination with energies above the energy gap. If the Γ -valley is slightly above the L-valley, emission from the Γ -valley becomes more pronounced at higher temperature, which is observed in Sample E. High density of states in the heavy holes (hh) valley in comparison with the lh valley in the case of large population also results in further increase of the emission blue shift. Similar results on the transition between indirect and direct bandgap emission with increase of temperature in Ge have previously been reported at temperatures $>300\text{K}$ ^{59–64}. The low temperature (160 K) observed in our experiment is explained as a close indirect-to-direct crossover point for the sample E.

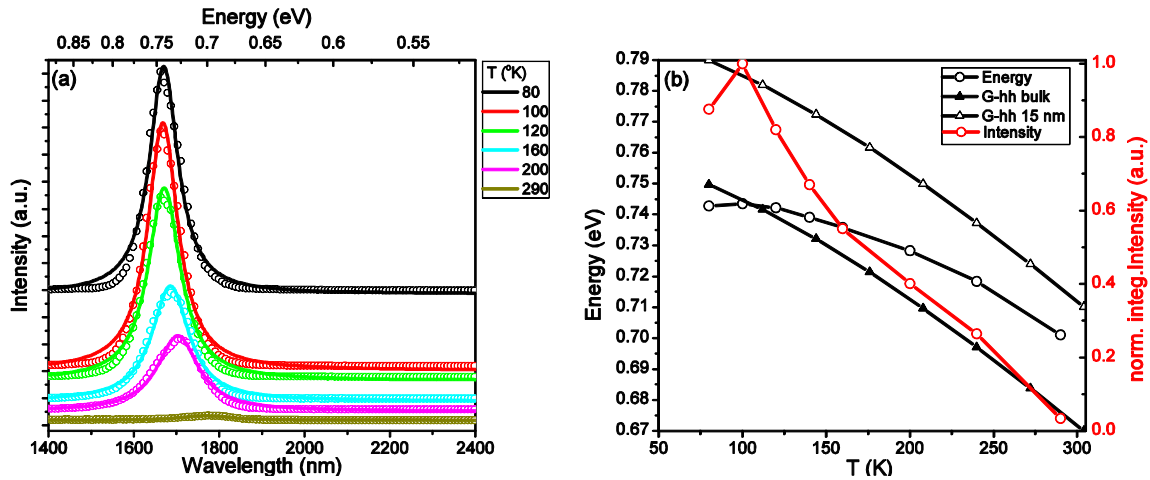


Figure 4. (a) Photoluminescence spectra of InGaAs/Ge/In_{0.29}Ga_{0.71}As/GaAs (Sample F) under $\epsilon=1.94\%$ biaxial tensile strain depending on temperature, (b) experimental (circles) and calculated (triangles) peak energy (black line) and normalised integrated intensity (red line) versus temperature.

Sample F (Table 1) has a structure of Ge/In_{0.29}Ga_{0.71}As/GaAs with the highest concentration of In in the buffer layer presented in this work. This concentration of In provides a biaxial tensile strain of $\epsilon=1.94\%$. The center of the PL peak at 80 K for sample F is at 0.739 eV (1678 nm). This emission corresponds to the Γ -hh transition which according to the 30 band k-p simulation (Fig. 8)

has energy 0.762 eV. It has been reported that experimental collection geometries normal to the sample surface (i.e. in the z direction) favour conduction band coupling with the hh valence band⁶⁵. This gives an additional credence to a pronounced blueshift of emission in the sample E. The high intensity of the Sample F emission is consistent with emission from the direct bandgap. It blue shifts by 40 meV (96 nm) at room temperature, providing temperature dependence of the Γ -valley. Spectra of the samples with varying tensile strain measured at T=80 K are summarised in Fig. 5 with intensity normalised to Sample F. It is clear that with increase of strain up to 1.6 % there is a red shift in sample emission, but for the sample F with the highest strain (1.94 %) its emission energy is higher than that of the unstrained sample A, which also proves a transition not to lh, but to hh. Relaxation of the strain in the sample F, which could be proposed to explain the blue shift of the emission, is not consistent with Sample F having the highest PL intensity of the discussed samples (see Fig. 5). Furthermore, the sample with the highest strain has the highest emission intensity, which is a feature of direct transition. Growth of a cap layer is known to result in marked improvements of the optical properties of semiconductor hetero- and nanostructures and this effect is usually associated with reduction in the large concentration of non-radiative defects (e.g., dangling bonds) usually present at the sample surface⁶⁶. In our studies, the difference in PL intensity for the capped and uncapped samples was about 30% in favor of uncapped structures (Figure A1 in the Appendix) so adding a capping layer is not reducing or increasing nonradiative recombination channels and not influencing carrier density in the Ge layer. (It is possible that the second interface between Ge and III-V material could generate additional defects in the QW).

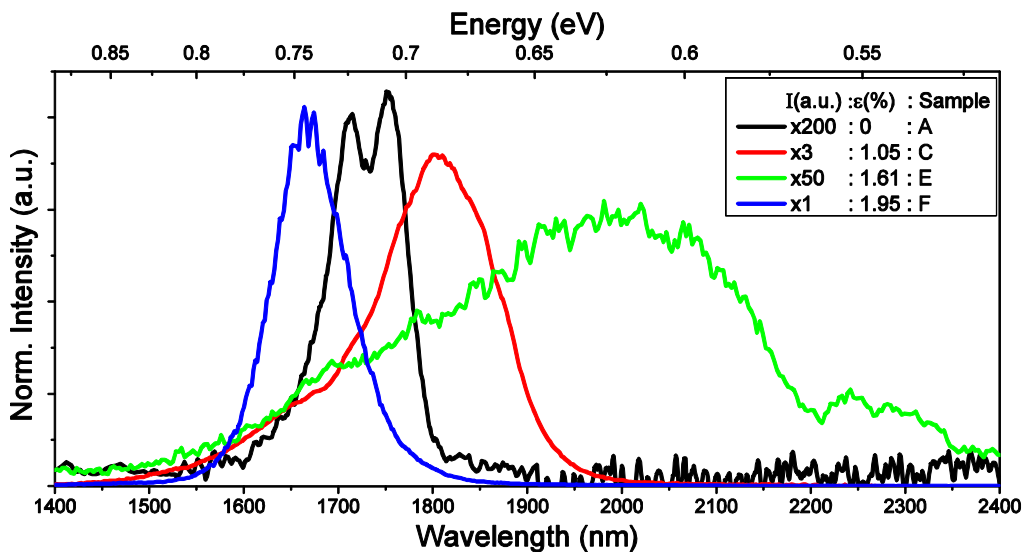


Figure 5. PL spectra at different biaxial tensile strain (Samples A, C, E, F) at 80 K.

B) Photoreflectance

For a closer examination of the tensile strain effect on the direct bandgap of Ge, the samples were studied with photoreflectance spectroscopy. Experimental PR spectra were fitted using two models: TDLS and complex Airy discussed previously. A high number of critical energies could improve fit quality however could also generate artificial peaks which compensate deviation of the model and experiment. To keep consistency between samples with different strain we used minimum number of critical energies in all fits: two critical energies to fit only major spectral features. In the end of this section there is a simulation of a PR spectra which includes all quantum levels of the 0.55-1.24 eV spectral range.

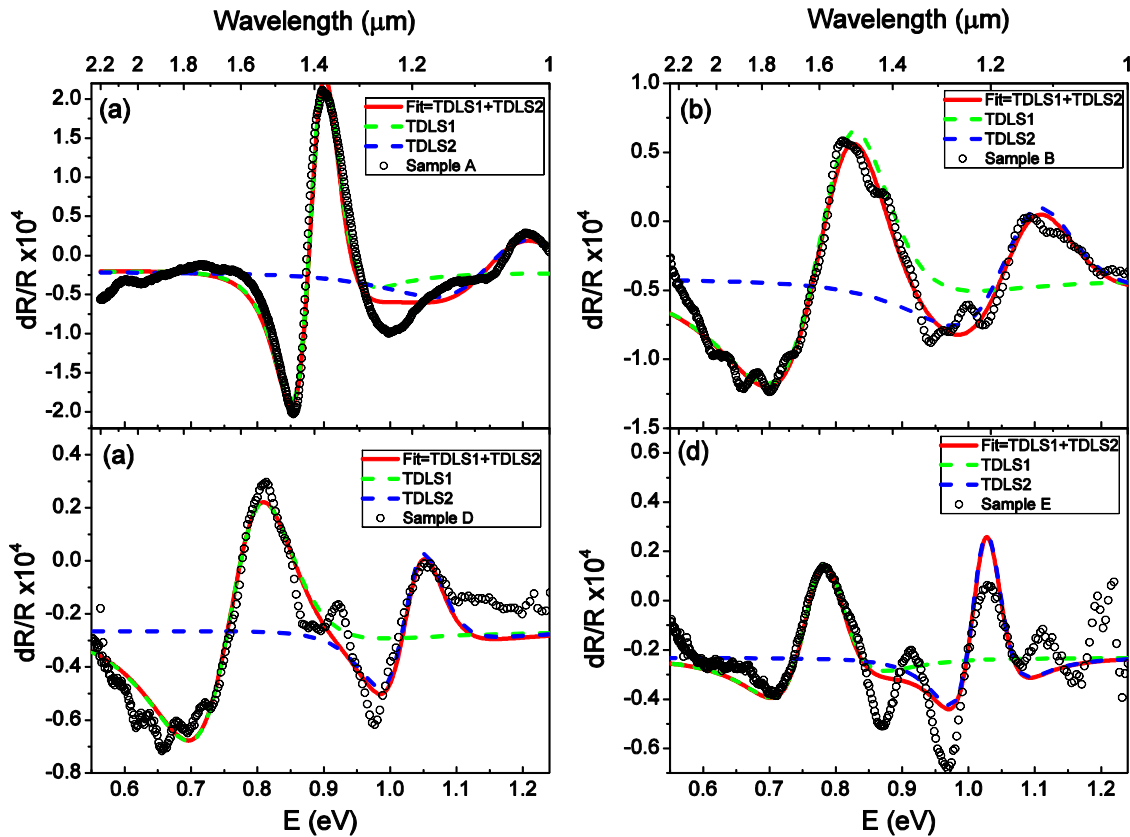


Figure 6. Photoreflectance spectrum of Ge under ϵ : (a) Sample A - 0 % (b) Sample B - 0.82% (c) Sample D - 1.11 % (d) Sample E - 1.6 % biaxial tensile strain at 80 K, fitted with 2 TDLS functions. Open circles correspond to the experimental data, red lines – fit including 2 TDLSs, depicted in green and blue respectively.

TDLS fits of PR spectra of the samples A, B, D, E are shown in Fig. 6(a)-(d) respectively. Since Seraphin-Bottka coefficients of a semiconductor are slowly changing with the wavelength^{67,68} we used the same φ parameter for all critical energies within a fit. Figure 6 has experimental points with the fitted curve overlaid including separate lines for each TDLS feature to indicate the

contribution of each. PR spectrum of the unstrained Ge sample A (Fig. 6 (a)) at 80 K provided a critical point at 0.889 eV, which is close to the theoretically expected value of Γ -hh transition equal to 0.881 meV . The critical point for the second TDLS feature was found at 1.183 eV, which is close to the predicted split-off band at 1.177 eV.

All PR critical energies are close to Γ -hh and split-off band transition energies obtained from k·p calculation (Fig. 8). The reason why Γ -hh transitions are seen rather than Γ -lh originates from higher electron-hole coupling for heavy holes over light holes⁶⁵ also mentioned in the PL discussion of sample E. For most of the spectra, some spectral features are visible at the expected values of the Γ -lh transition, however these are too faint to make a clear assignment of a signal from this transition or obtain a reliable fit.

These weak oscillations are particularly noticeable in Fig. 6(b) for the sample B with 0.82 % of strain. Notwithstanding the possibility of sub-band transitions, these most likely originate from Fabry-Perot oscillations of the light in the optical cavity created between the top and bottom edges of the sample structure. Thin layers create interference of the light which can affect the spectral shape⁶⁹ and in some cases can generate a destructive interference of the PR signal. The absence of a signal corresponding to emission from the L-band in the PR spectra of the thick unstrained Ge (sample A) adds further credence to this hypothesis. With increasing strain, the critical energy obtained from the fitting exhibits a red shift as expected from the k·p simulation.

Sample D with Ge under 1.11 % strain (Fig. 6(c)) was grown without a cap layer on top of the Ge. Critical energies corresponding to Γ -hh and split-off band in this case are found to be 0.780 eV and 1.033 eV. Capped samples C and F (Table 1), as well as others not presented in this work, did not give any detectable PR response from Ge. This originates from the fact that perturbation of the semiconductor by the reflected laser light reduces exponentially with the depth of the material. Besides that Ge PR response is created from perturbation of the surface states of Ge which do not present in the capped samples.

PR spectra of sample E (Table 1) with $\epsilon = 1.6$ % tensile strain is presented in Fig. 6(d). The critical points for this sample are at 0.778 eV and 1.023 eV. The spectral feature in between these critical points could correspond to an additional critical point, however a similar feature is observed in the unstrained sample A between Γ -hh and split-off band (Fig. 6(a)) with no sub-band transition that can be attributed to this energy. So deviation between the theoretical model and the experimentally

fitted data can be also attributed not to another sub-band energy, but to imperfection of the TDLS model.

Table 2. TDLS fit parameters.

Sample	Strain, ε (%)	Function	Amplitude, C	Phase, φ (rad)	Broadening, Γ (eV)	Energy, E (eV)
A	0	TDLS 1	-4.781e-08	3.798	0.05907	0.889
		TDLS 2	2.882e-07	3.798	0.1617	1.174
		offset	-2.236e-05			
B	0.82	TDLS 1	2.546e-07	3.970	0.147	0.806
		TDLS 2	2.212e-07	3.970	0.148	1.084
		offset	-4.25e-05			
D	1.11	TDLS 1	8.223e-08	3.704	0.131	0.780
		TDLS 2	1.789e-08	3.704	0.078	1.033
		offset	-2.680e-05			
E	1.6	TDLS 1	1.454e-08	4.379	0.085	0.778
		TDLS 2	1.162e-08	4.379	0.060	1.023
		offset	-2.324e-05			

All fitting parameters for TDLS fits are summarised in Table 2. With an increase of strain, there is an expected red shift for the first critical point in energy from 0.89 eV for the unstrained sample (sample A) to 0.78 eV for the 1.6 % tensile strained sample (sample E).

Since TDLS model shows some deviation with the experiment, an Airy fit for the samples A, B, D and E is also performed (Fig. 7 (a)-(d)). Similar to TDLS each fit was performed for 2 critical points. Since perturbation is the same for all energy levels, the $\hbar\theta$ parameter for both critical points is also equal. All Airy fit parameters can be found in Table A1 of the Appendix. One can see that for samples B and E fitting parameter $\hbar\theta < \Gamma/3$ which means they are in the low-field regime, while for samples A and D $\hbar\theta \sim \Gamma$ which corresponds to the intermediate-field measurements. Effective built-in electric field was also estimated from the $\hbar\theta$ parameter and mobility μ . It should be noted that Sample B has a lower value of effective built-in electric field (310 kV/cm) then that of Sample A (153 kV/cm). For this reason, a clear selection of either TDLS or Airy functions for

photoreflectance spectra based on the value of $\hbar\theta$ is not possible in our case. Comparing the quality of TDLS and Airy fit one can note a better coverage of Airy fits for the Samples A and E. There is almost no difference for the samples B and D. Critical points of Airy and TDLS fits in addition to PL peak points are shown on the top of theoretically calculated band energies in Fig. 8.

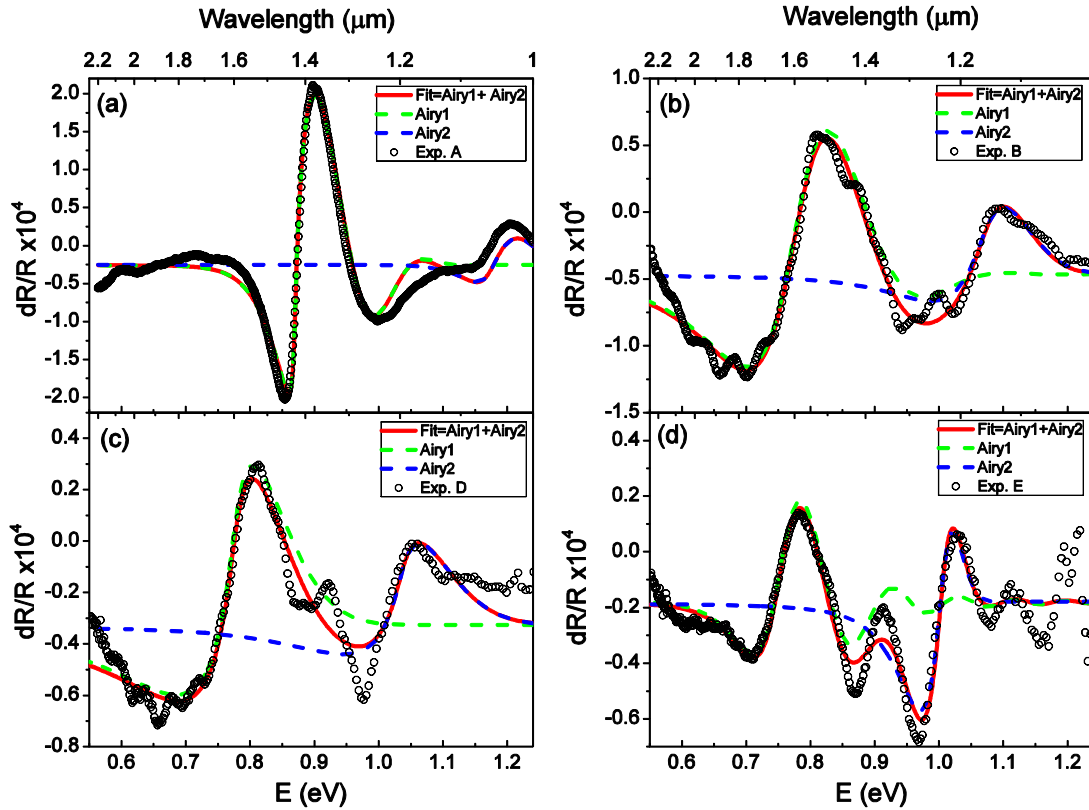


Figure 7. Photoreflectance spectrum of Ge under ε : (a) 0 % (b) 0.82 % (c) 1.11 % (d) 1.6 % biaxial tensile strain at 80 K, fitted with 2 Airy functions. Dotted lines corresponds to the experimental data, red lines – fit including 2 Airy functions, depicted in green and blue respectively.

TDLS critical points of the samples A, B, D, E follows the trend of the theoretically calculated Γ -hh in Fig. 8. In addition to this PL peak of the sample F follows the trend of the PR critical points. Taking into account increase of PL intensity (see Fig. 5) this gives an additional confirmation of the direct bandgap nature of PL emission from the sample with the highest strain. The photoreflectance spectrum contains information on all critical points of the band structure. Due to quantum confinement in the thin Ge layer, electron and hole energy levels are situated not at the band edge, but at a number of sub-band energy levels. This affects the quality of fitting in Figs. 6 and 7. To make a PR model that includes all quantum energy levels, the TDLS parameters for all sub-bands are calculated directly.

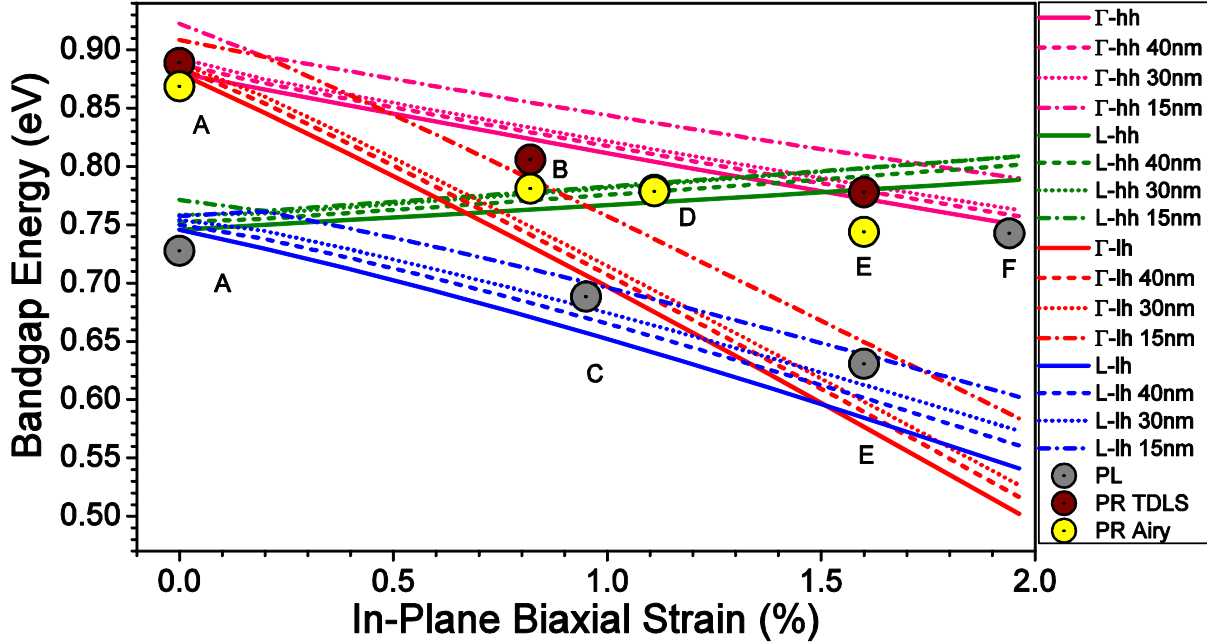


Figure 8. Theoretical bandgap-strain dependence for Ge calculated using a 30×30 k-p model taking into account quantisation-induced bandgap enhancement at decreased ϵ -Ge layer thicknesses for 40 nm, 30 nm and 15 nm quantum wells. Experimental peaks given by PL and PR data are shown as circles over theoretically predicted transitions from Γ - and L- valley to light (lh) and heavy (hh) holes.

The optical coupling, given by the square of the momentum matrix element between the electron-hole wave functions is used as a relative amplitude parameter for each critical point. Density of states (DOS) is related to charge carriers lifetime and thus is taken as a broadening with a general scaling coefficient for all sub-band energies. Sub-band energies, DOS and broadening (Figure A2 in the Appendix) are calculated for 40 nm quantum confinement for $\epsilon=0.82$ % biaxial tensile strain and for 30 nm quantum confinement for $\epsilon=1.11$ %. Phase parameters are calculated from Seraphin-Bottka coefficients (Figure A3 in the Appendix), assuming equality of $e^{i\phi}$ terms in Airy and TDLS functions. The resulting TDLS functions are obtained from the model and are depicted in Fig. 9. As seen from those graphs PR model of 0 %, 0.82 % and 1.11% of biaxial tensile strain corresponds to experimental Samples A, B and D (Table 1). There are number of assumptions done during this simulation, such as ideal surface of Ge quantum well, homogeneous strain within Ge layer as well as general TDLS simplifications. We also simulated Seraphin Bottka coefficients without including quantum constrains. This simplifications effect on the simulation quality, however this simulation gives number of features visible in the experimental spectra and has quality comparable with the other⁷⁰. I should also mention certain deficit of PR spectra simulations even though PR spectra require careful interpretation.

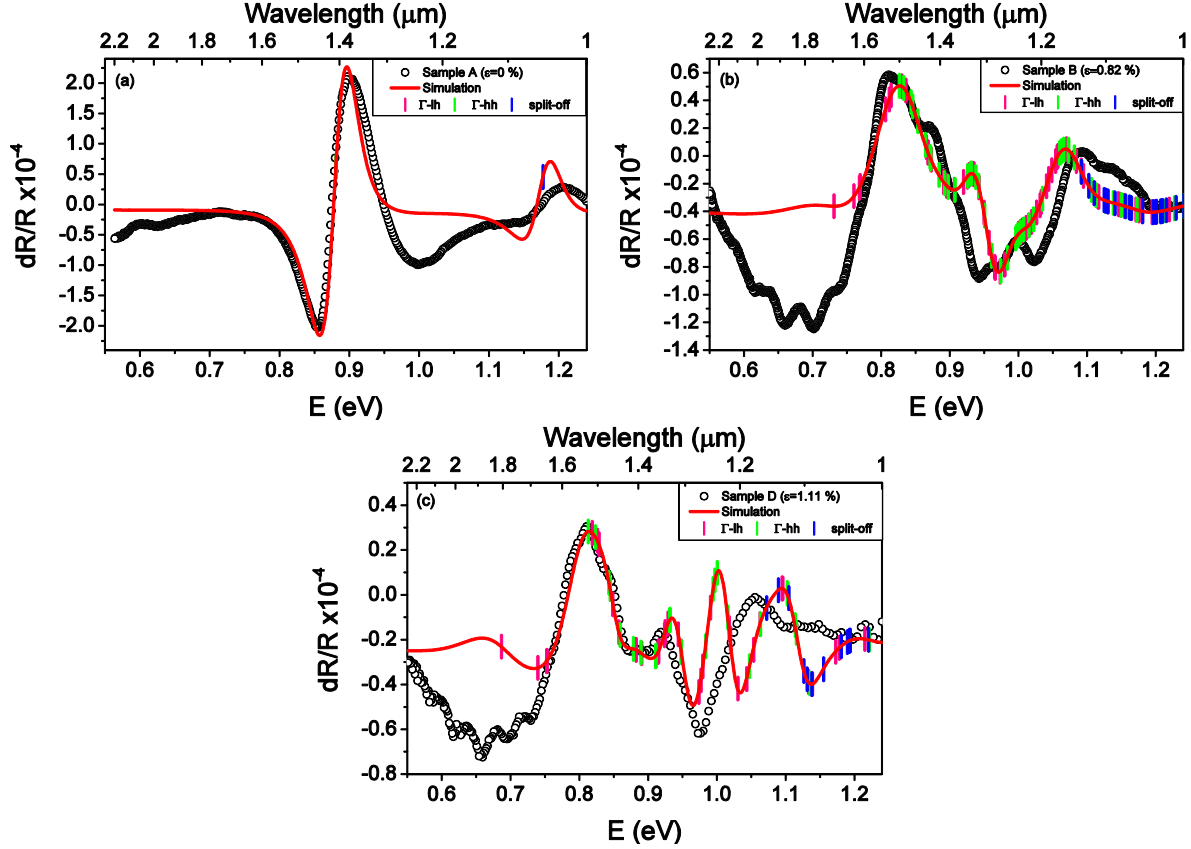


Figure 9. Full photoreflectance spectra simulation on the top of experimental data for (a) unstrained sample (b) $\epsilon=0.82\%$ model over sample D spectra (c) $\epsilon=1.11\%$ model over sample E spectra. Γ -lh, Γ -hh and split-off sub-band transition energies are depicted as a vertical dashes.

Conclusions

In this article, we discussed the band structure of germanium under tensile strain. Utilising k - p modelling band transitions were calculated numerically and then confirmed in the experimental study. Using photoluminescence, the indirect L valley was determined at various strain and temperatures. The photoreflectance identified the change of direct bandgap with increase of strain and confirmed theoretical assumptions about high heavy hole coupling in germanium. Photoreflectance spectra were analysed using TDLS and FKO models and compared with a simulated photoreflectance spectra. The TDLS approximation fit had the advantage in obtaining energy values close to the Γ -hh and split-off transition energies obtained from k - p simulation, while the Airy fit showed better coverage of the experimental data. The indirect to direct crossover was reached in this study between the samples with 1.6 % and 1.94 % lattice mismatch of Ge and InGaAs layers.

Acknowledgments

Thanks to David Williams for the discussions during preparation of this paper. GGD and MG acknowledge the use of computational facilities at the Atomistic Simulation Centre in Queen's University Belfast and the support from the Department for the Employment of Northern Ireland. The research in this publication was supported under the US-Ireland R&D Partnership Program by Science Foundation Ireland (SFI) Grant No. SFI/14/US/I3057, by InvestNI Grant No. USI-073, by the National Science Foundation (US) Grant No. ECCS-1348653 and ECCS-1507950.

References

- ¹ D.A.B. Miller, *J. Optoelectron.* **11**, 155 (1997).
- ² K. Ohashi, K. Nishi, T. Shimizu, M. Nakada, J. Fujikata, J. Ushida, S. Toru, K. Nose, M. Mizuno, H. Yukawa, M. Kinoshita, N. Suzuki, A. Gomyo, T. Ishi, D. Okamoto, K. Furue, T. Ueno, T. Tsuchizawa, T. Watanabe, K. Yamada, S.I. Itabashi, and J. Akedo, *Proc. IEEE* **97**, 1186 (2009).
- ³ D.A.B. Miller, *Proc. IEEE* **97**, 1166 (2009).
- ⁴ C. Gunn, *IEEE Micro* **26**, 58 (2006).
- ⁵ L. Liu, R. Kumar, K. Huybrechts, T. Spuesens, G. Roelkens, E.-J. Geluk, T. de Vries, P. Regreny, D. Van Thourhout, R. Baets, and G. Morthier, *Nat. Photonics* **4**, (2010).
- ⁶ A.W. Fang, H. Park, O. Cohen, R. Jones, M.J. Paniccia, and J.E. Bowers, *Opt. Express* **14**, 9203 (2006).
- ⁷ J. Van Campenhout, R.P. Rojo, P. Regreny, C. Seassal, D. Van Thourhout, S. Verstuyft, L. Di Cioccio, J.-M. Fedeli, C. Lagahe, and R. Baets, *Opt. Express* **15**, 6744 (2007).
- ⁸ M. Lebby, S. Ristic, N. Calabretta, and R. Stabile, in *Opt. Interconnects Data Centers* (Elsevier, 2017), pp. 97–120.
- ⁹ J.-M. Fedeli, B. Bakir, and N. Olivier, *Proc. SPIE* **7942**, 79420O (2011).
- ¹⁰ Z. Wang, B. Tian, M. Pantouvaki, W. Guo, P. Absil, J. Van Campenhout, C. Merckling, and D. Van Thourhout, *Nat. Photonics* **9**, 837 (2015).
- ¹¹ S. Wirths, R. Geiger, N. von den Driesch, G. Mussler, T. Stoica, S. Mantl, Z. Ikonik, M. Luysberg, S. Chiussi, J.M. Hartmann, H. Sigg, J. Faist, D. Buca, and D. Grützmacher, *Nat. Photonics* **9**, 88 (2015).
- ¹² S. Gupta, B. Magyari-Köpe, Y. Nishi, and K.C. Saraswat, *J. Appl. Phys.* **113**, (2013).
- ¹³ S. Biswas, J. Doherty, D. Saladukha, Q. Ramasse, D. Majumdar, M. Upmanyu, A. Singha, T.

- Ochalski, M.A. Morris, and J.D. Holmes, *Nat. Commun.* **7**, 11405 (2016).
- ¹⁴ R. a. Soref and L. Friedman, *Superlattices Microstruct.* **14**, 189 (1993).
- ¹⁵ P.H. Lim, S. Park, Y. Ishikawa, and K. Wada, *Opt. Express* **17**, 16358 (2009).
- ¹⁶ K. Wang, Q. Gong, H. Zhou, C. Kang, J. Yan, Q. Liu, and S. Wang, *Appl. Surf. Sci.* **291**, 45 (2014).
- ¹⁷ M. V. Fischetti and S.E. Laux, *J. Appl. Phys.* **80**, 2234 (1996).
- ¹⁸ F. Murphy-Armando and S. Fahy, *J. Appl. Phys.* **109**, (2011).
- ¹⁹ D. Mohata, S. Mookerjee, A. Agrawal, Y. Li, T. Mayer, V. Narayanan, A. Liu, D. Loubychyev, J. Fastenau, and S. Datta, *Appl. Phys. Express* **4**, (2011).
- ²⁰ D. Rideau, M. Feraille, L. Ciampolini, M. Minondo, C. Tavernier, H. Jaouen, and A. Ghetti, *Phys. Rev. B - Condens. Matter Mater. Phys.* **74**, 1 (2006).
- ²¹ M.S. Hybertsen and S.G. Louie, *Phys. Rev. B* **34**, 5390 (1986).
- ²² Y.P. Varshni, *Physica* **34**, 149 (1967).
- ²³ N. Pavarelli, T.J. Ochalski, F. Murphy-Armando, Y. Huo, M. Schmidt, G. Huyet, and J.S. Harris, *Phys. Rev. Lett.* **110**, 1 (2013).
- ²⁴ W.A. Harrison, *J. Appl. Phys.* **110**, (2011).
- ²⁵ S. Paul, J.B. Roy, and P.K. Basu, *J. Appl. Phys.* **69**, 827 (1991).
- ²⁶ W. Kohn and L.J. Sham, *Phys. Rev.* **140**, A1133 (1965).
- ²⁷ J.P. Perdew and Y. Wang, *Phys. Rev. B* **45**, 244 (1992).
- ²⁸ P. Giannozzi, S. Baroni, N. Bonini, M. Calandra, R. Car, C. Cavazzoni, D. Ceresoli, G.L. Chiarotti, M. Cococcioni, I. Dabo, A. Dal Corso, S. de Gironcoli, S. Fabris, G. Fratesi, R. Gebauer, U. Gerstmann, C. Gougoussis, A. Kokalj, M. Lazzeri, L. Martin-Samos, N. Marzari, F. Mauri, R. Mazzarello, S. Paolini, A. Pasquarello, L. Paulatto, C. Sbraccia, S. Scandolo, G. Sclauzero, A.P. Seitsonen, A. Smogunov, P. Umari, and R.M. Wentzcovitch, *J. Phys. Condens. Matter* **21**, 395502 (2009).
- ²⁹ A. Marini, C. Hogan, M. Grüning, and D. Varsano, *Comput. Phys. Commun.* **180**, 1392 (2009).
- ³⁰ S. Botti, F. Sottile, N. Vast, V. Olevano, L. Reining, H.C. Weissker, A. Rubio, G. Onida, R. Del Sole, and R.W. Godby, *Phys. Rev. B* **69**, 1 (2004).
- ³¹ J.A. Berger, *Phys. Rev. Lett.* **115**, 1 (2015).
- ³² M. Fox, *Optical Properties of Solids* (Oxford University Press, 2001).

- ³³ R.J. Bondi, S. Lee, and G.S. Hwang, *ACS Nano* **5**, 1713 (2011).
- ³⁴ S.T. Sundari and G. Raghavan, *Appl. Phys. Lett.* **86**, 1 (2005).
- ³⁵ P.D. Nguyen, M.B. Clavel, P.S. Goley, J.-S. Liu, N.P. Allen, L.J. Guido, and M.K. Hudait, *IEEE J. Electron Devices Soc.* **3**, 341 (2015).
- ³⁶ S.M. Ting and E.A. Fitzgerald, *J. Appl. Phys.* **87**, 2618 (2000).
- ³⁷ M.K. Hudait and S.B. Krupanidhi, *J. Appl. Phys.* **89**, 5972 (2001).
- ³⁸ M.B. Clavel and M.K. Hudait, *IEEE Electron Device Lett.* **38**, 1196 (2017).
- ³⁹ M. Clavel, D. Saladukha, P.S. Goley, T.J. Ochalski, F. Murphy-Armando, R.J. Bodnar, and M.K. Hudait, *ACS Appl. Mater. Interfaces* **7**, 26470 (2015).
- ⁴⁰ M. Clavel, P. Goley, N. Jain, Y. Zhu, and M.K. Hudait, *IEEE J. Electron Devices Soc.* **3**, 184 (2015).
- ⁴¹ R.N. Bhattacharya, H. Shen, P. Parayanthal, F.H. Pollak, T. Coutts, and H. Aharoni, *Phys. Rev. B* **37**, 4044 (1988).
- ⁴² L. V. Keldysh, *J. Exptl. Theor. Phys.* **33**, 994 (1957).
- ⁴³ J.P. Estrera, W.M. Duncan, and R. Glosser, *Phys. Rev. B* **49**, 7281 (1994).
- ⁴⁴ B.O. Seraphin and N. Bottka, *Phys. Rev.* **145**, 628 (1966).
- ⁴⁵ D.E. Aspnes, *Phys. Rev.* **147**, 554 (1966).
- ⁴⁶ R.A. Batchelor, A.C. Brown, and A. Hamnett, *Phys. Rev. B* **41**, 1401 (1990).
- ⁴⁷ D.E. Aspnes, *Surf. Sci.* **37**, 418 (1973).
- ⁴⁸ K. Zelazna, M.P. Polak, P. Scharoch, J. Serafinczuk, M. Gladysiewicz, J. Misiewicz, J. Dekoster, and R. Kudrawiec, *Appl. Phys. Lett.* **106**, 142102 (2015).
- ⁴⁹ M.E. Ziffer, J.C. Mohammed, and D.S. Ginger, *ACS Photonics* **3**, 1060 (2016).
- ⁵⁰ R. Nedzinskas, B. Cechavicius, J. Kavaliauskas, V. Karpus, G. Valusis, L.H. Li, S.P. Khanna, and E.H. Linfield, *Nanoscale Res. Lett.* **7**, 609 (2012).
- ⁵¹ D.E. Aspnes and A. Frova, *Solid State Commun.* **88**, 1061 (1993).
- ⁵² S. Koeppen and P. Handler, *Phys. Rev.* **187**, 1182 (1969).
- ⁵³ R.R. Lieten, K. Bustillo, T. Smets, E. Simoen, J.W. Ager, E.E. Haller, and J.P. Locquet, *Phys. Rev. B* **86**, 1 (2012).
- ⁵⁴ M. Virgilio, C.L. Manganelli, G. Grosso, T. Schroeder, and G. Capellini, *J. Appl. Phys.* **114**, (2013).

- ⁵⁵ Yan Cai, Zhaohong Han, Xiaoxin Wang, R.E. Camacho-Aguilera, L.C. Kimerling, J. Michel, and Jifeng Liu, *IEEE J. Sel. Top. Quantum Electron.* **19**, 1901009 (2013).
- ⁵⁶ G. Pizzi, M. Virgilio, and G. Grosso, *Nanotechnology* **21**, 55202 (2010).
- ⁵⁷ V. Soriano, A. Perna, L. Colace, G. Assanto, H.C. Luan, and L.C. Kimerling, *Appl. Phys. Lett.* **93**, 93 (2008).
- ⁵⁸ J. Liu, X. Sun, L.C. Kimerling, and J. Michel, *Opt. Lett.* **34**, 1738 (2009).
- ⁵⁹ T.H. Cheng, C.Y. Ko, C.Y. Chen, K.L. Peng, G.L. Luo, C.W. Liu, and H.H. Tseng, *Appl. Phys. Lett.* **96**, (2010).
- ⁶⁰ G. Grzybowski, R. Roucka, J. Mathews, L. Jiang, R.T. Beeler, J. Kouvetakis, and J. Menéndez, *Phys. Rev. B* **84**, 205307 (2011).
- ⁶¹ H.M. van Driel, A. Elci, J.S. Bessey, and M.O. Scully, *Solid State Commun.* **20**, 837 (1976).
- ⁶² W. Klingenstein and H. Schweizer, *Solid State Electron.* **21**, 1371 (1978).
- ⁶³ S. Manna, a Katiyar, R. Aluguri, and S.K. Ray, *J. Phys. D. Appl. Phys.* **48**, 215103 (2015).
- ⁶⁴ Y. Huo, H. Lin, R. Chen, M. Makarova, Y. Rong, M. Li, T.I. Kamins, J. Vuckovic, and J.S. Harris, *Appl. Phys. Lett.* **98**, 96 (2011).
- ⁶⁵ J.R. Sanchez-Perez, C. Boztug, F. Chen, F.F. Sudradjat, D.M. Paskiewicz, R. Jacobson, M.G. Lagally, and R. Paiella, *Proc. Natl. Acad. Sci.* **108**, 18893 (2011).
- ⁶⁶ H. Saito, K. Nishi, and S. Sugou, *Appl. Phys. Lett.* **73**, 2742 (1998).
- ⁶⁷ M. Cardona, K.L. Shaklee, and F.H. Pollak, *Phys. Rev.* **154**, 696 (1967).
- ⁶⁸ H.R. Philipp and E.A. Taft, *Phys. Rev.* **113**, 1002 (1959).
- ⁶⁹ R.A. Batchelor and A. Hamnett, *J. Appl. Phys.* **71**, 2414 (1992).
- ⁷⁰ O.L. Lazarenkova and A.N. Pikhtin, *Phys. Status Solidi* **175**, 51 (1999).

Appendix

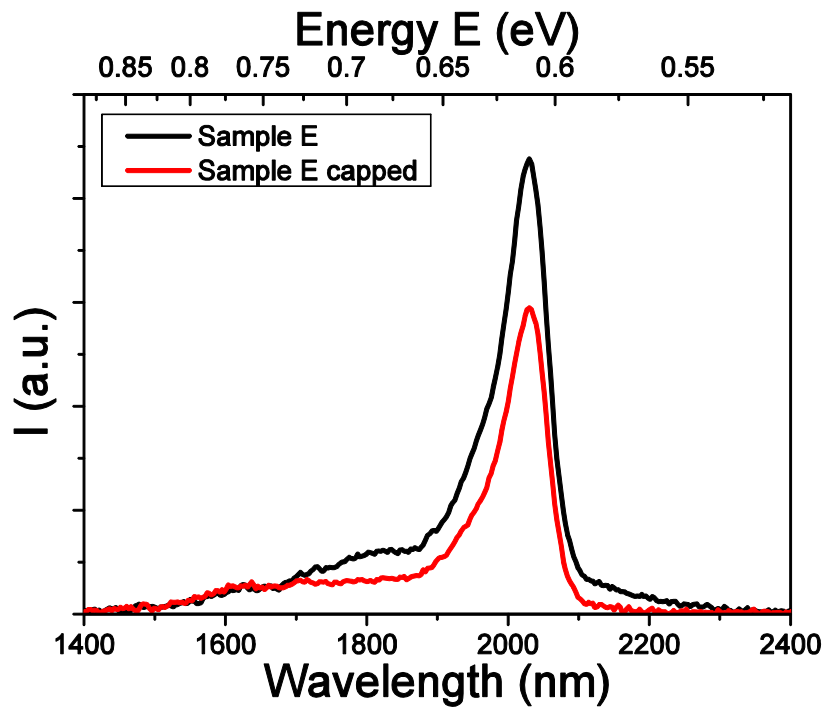


Figure A1. Photoluminescence spectra of Ge/In_{0.24}Ga_{0.76}As/GaAs (Sample E) and InGaAs/Ge/In_{0.24}Ga_{0.76}As/GaAs (Sample E capped) under $\epsilon=1.6\%$ biaxial tensile strain at 8K

Table A1. Airy fit parameters.

Sample	Strain, ϵ (%)	Function	Amplitude C (a.u.)	Phase, φ (rad)	Pertur- bation, $\hbar\theta$ (eV)	Efficient Built-in Electric Field, \mathcal{E}_{eff} (kV/cm)	Batchelor, δ (eV ⁻¹)	Broadening, Γ (eV)	Energy, E (eV)
A	0	Airy 1	0.001003	2.965	0.06928	153.40	11.23	0.05013	0.8687
		Airy 2	0.0005207	2.965	0.06928		0	0.2844	1.170
		offset	-2.559e-05						
B	0.82	Airy 1	0.002095	1.706	0.1095	309.66	2.137	0.5292	0.7811
		Airy 2	0.0009086	1.706	0.1095		7.266	0.3495	1.081
		Offset	-4.611e-05						
D	1.11	Airy 1	0.0003073	2.034	0.1555	526.89	11.09	0.1283	0.7786
		Airy 2	-0.0002524	2.034	0.1555		11.79	0.1224	1.039
		offset	-3.264e-05						
E	1.6	Airy 1	0.0006077	1.972	0.06432	141.44	0	0.5670	0.7440
		Airy 2	-0.001164	1.972	0.06432		25.53	0.4594	1.015
		offset	-1.803e-05						

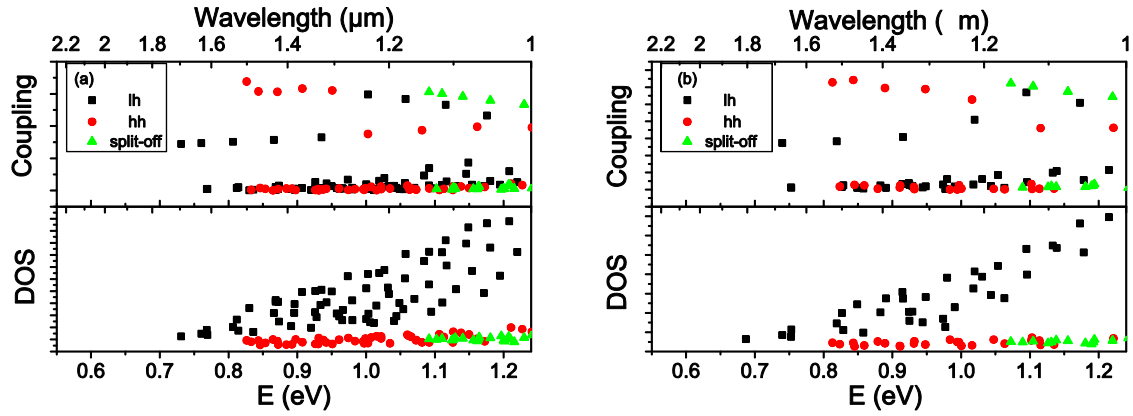


Figure A2. k - p calculations of electron-hole wavefunction coupling and density of states (DOS) for sub-band transition energies in (a) 40nm Ge quantum well with $\epsilon=0.82\%$ biaxial tensile strain (b) 30nm Ge quantum well with $\epsilon=1.11\%$ biaxial tensile strain.

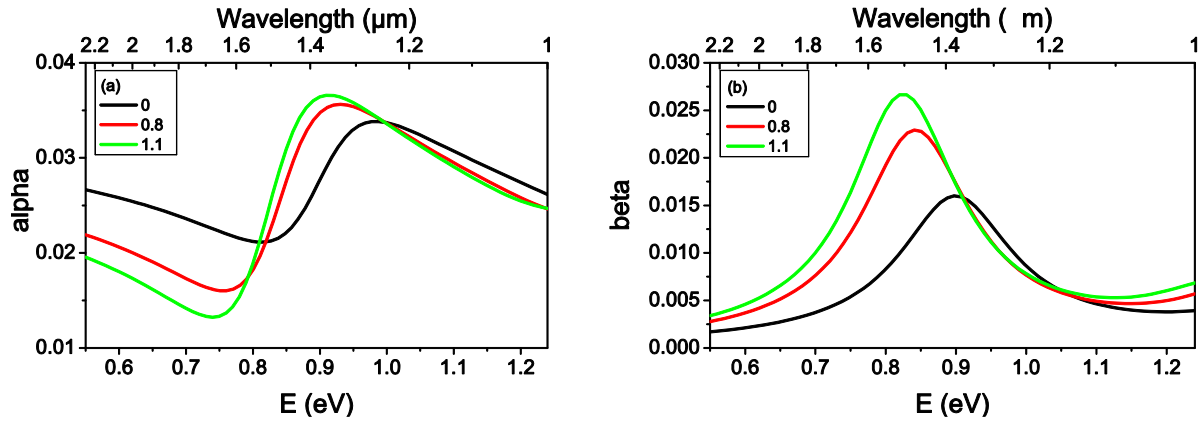


Figure A3. Calculated (a) α and (b) β Seraphin-Bottka coefficients in Ge at 80K and at 0 %, 0.8 % and 1.1 % biaxial tensile strain.